# Probing Neutral Triple Gauge Couplings via $Z\gamma\,(\ell^+\ell^-\gamma)$ Production at $e^+e^-$ Colliders

**Danning Liu**[1,2], **Rui-Qing Xiao**[1,2,3], **Shu Li**[1,2,4], **John Ellis**[3,5,1], **Hong-Jian He**[1,2,4], **Rui Yuan**[1,2]

[1] Tsung-Dao Lee Institute, Shanghai Jiao Tong University, Shanghai, China
[2] School of Physics and Astronomy, Key Laboratory for Particle Astrophysics and Cosmology, Shanghai Key Laboratory for Particle Physics and Cosmology, Shanghai Jiao Tong University, Shanghai, China
[3] Department of Physics, King's College London, Strand, London WC2R 2LS, UK
[4] Center for High Energy Physics, Peking University, Beijing, China
[5] Theoretical Physics Department, CERN, CH-1211 Geneva 23, Switzerland

`danningliu@sjtu.edu.cn`, `xiaoruiqing@sjtu.edu.cn`, `shuli@sjtu.edu.cn`, `john.ellis@cern.ch`, `hjhe@sjtu.edu.cn`, `yuanrui@sjtu.edu.cn`

**Abstract**

Neutral triple gauge couplings (nTGCs) are absent in the Standard Model (SM) and at the dimension-6 level in the Standard Model Effective Field Theory (SMEFT), arising first from dimension-8 operators. As such, they provide a unique window for probing new physics beyond the SM. These dimension-8 operators can be mapped to nTGC form factors whose structure is consistent with the spontaneously-broken electroweak gauge symmetry of the SM. In this work, we study the probes of nTGCs in the reaction $e^+e^-\to Z\gamma$ with $Z\to\ell^+\ell^-$ $(\ell=e,\mu)$ at an $e^+e^-$ collider. We perform a detector-level simulation and analysis of this reaction at the Circular Electron Positron Collider (CEPC) with collision energy $\sqrt{s}=240\,\text{GeV}$ and an integrated luminosity of $5\,\text{ab}^{-1}$. We present the sensitivity limits on probing the new physics scales of dimension-8 nTGC operators via measurements of the corresponding nTGC form factors.

KCL-PH-TH/2024-18, CERN-TH-2024-046

## Contents



# 1 Introduction

The Standard Model Effective Field Theory (SMEFT) [1] is a powerful framework for studying model-independently possible new physics beyond the Standard Model (SM). The SMEFT includes only the known elementary particles, which are assumed to have the SM quantum numbers and thus have the interactions with mass-dimension $d \leqslant 4$ that are predicted by the SM, but the SMEFT also includes additional effective interactions with mass-dimensions $d > 4$. Such higher-dimensional interactions could arise from new physics at energy scales beyond the electroweak scale due to possible exchanges of new massive particles and/or novel strong dynamics. The SMEFT interactions with dimension 5 may be relevant for neutrino physics, whereas collider experiments are generally sensitive to SMEFT interactions with even dimensions $d \geqslant 6$. Probing the effects of SMEFT operators may either constrain the possible high-scale new physics dynamics or provide hints to its possible nature, without assuming the ultraviolet (UV) origin or making any assumptions about its form.

There is an extensive theoretical literature classifying the SMEFT operators of dimension 6 [2, 3] and above [4, 5], and a growing number of phenomenological and experimental papers analyzing the constraints on their possible coefficients that are imposed by current data from the LHC and elsewhere. Most of these analyses have had operators with $d = 6$ as their primary focus, often working to linear order in the SMEFT operator coefficients, i.e., quadratically in the new physics scale, an approximation that takes into account their interferences with SM interactions [6, 7, 8, 9, 10]. To date there is no significant indication that any $d = 6$ SMEFT operator has a non-zero coefficient, but future colliders will provide much greater precision in SMEFT probes [11, 12, 13, 14].

A complete analysis of the phenomenology of dimension-6 operators should include their quadratic effects on event rates, which depend quartically on the new physics scale. At this level one should in general consider the effects of linear interference between dimension-8 SMEFT operators and SM amplitudes, which also depend quartically on the new physics scale, and there is a growing literature of analyses that take these into account [15, 16, 17, 18, 19]. Complementing these studies, it is interesting to consider processes that have no dimension-6 operator contributions, to which dimension-8 operators make the leading SMEFT contributions. These processes include quartic neutral vector-boson interactions and also neutral triple gauge couplings (nTGCs), where the nTGCs are the object of the present study.

Neutral triple gauge couplings are absent in the SM and at the level of dimension-6 operators in the SMEFT, arising first at the level of dimension-8 operators [20]. Hence nTGCs can provide a unique window for probing new physics beyond the SM [21, 22, 23, 24]. The most direct experimental probes of nTGCs are via measurements of the corresponding form factors. A consistent formulation of nTGC form factors has recently been proposed, which matches precisely the nTGC form factors with the gauge-invariant dimension-8 effective operators of the SMEFT [23, 24]. This imposes nontrivial relations among the nTGC form factors and gives correct predictions for the contributions of the nTGC form factors to high-energy scattering amplitudes [23, 24]. These theoretical papers investigated probes of the nTGCs at both the electron-positron and hadron colliders.

In this work, we study experimental probes of the dimension-8 nTGC operators via measurements of their corresponding nTGC form factors in the reaction $e^+e^- \to Z\gamma$ process with $Z \to \ell^+\ell^-$ ($\ell = e, \mu$) decays, as shown in Fig. 1. For this purpose we perform detector-level simulation and analysis of nTGCs at the Circular Electron Positron Collider (CEPC) with energy $\sqrt{s} = 240$ GeV and an integrated luminosity of 5 ab$^{-1}$, using a model-independent approach that could also be adopted for other experiments.

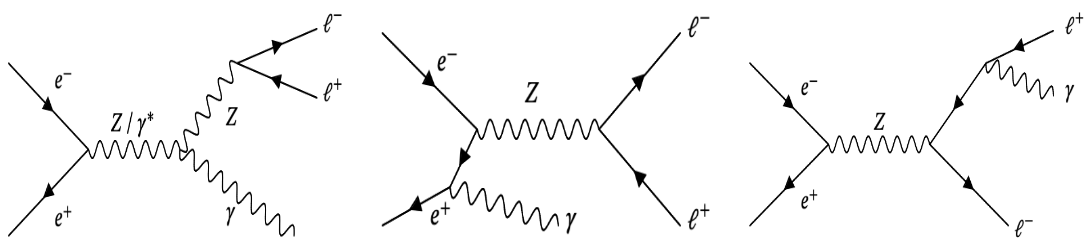


Figure 1: Feynman diagrams that contribute to the reaction $e^+e^- \to Z\gamma$. The first diagram is the signal process containing the nTGC vertex $Z^*Z\gamma$ or $\gamma^*Z\gamma$; the second and third diagrams show the SM background contributions with initial-state-radiation photon or final-state-radiation photon.

This work is organized as follows. In Section 2, we first describe the theoretical framework for the nTGCs, which includes the SMEFT formulation of the dimension-8 nTGC operators and the corresponding nTGC form factors. Then, we present a detector-level simulation and analysis for the dimension-8 nTGC effective operators and the nTGC form factors via the reaction $e^+e^- \to Z\gamma$, using the CEPC detector as a benchmark. In Section 3, we analyze the uncertainties for both the signals and backgrounds. After this, we present our results in Section 4 for the sensitivities on probing the nTGCs at the CEPC. Finally, we conclude in Section 5.

## 2 Theoretical Framework, Simulation and Analysis

In this Section we first present the theoretical framework for the nTGCs, including both the SMEFT formulation with dimension-8 nTGC operators and the corresponding nTGC form factors. Then, we systematically perform a detector-level simulation and analysis for the dimension-8 nTGC effective operators and the corresponding nTGC form factors via the reaction $e^+e^-\!\to Z\gamma$, using the CEPC as a benchmark.

### 2.1 Theoretical Framework for the nTGCs

The dimension-8 SMEFT effective Lagrangian takes the following form:

$$\mathcal{L}_{\text{SMEFT}} = \sum_j \frac{c_j}{\Lambda^4}\mathcal{O}_j = \sum_j \frac{\text{sign}(c_j)}{\Lambda_j^4}\mathcal{O}_j\,, \tag{1}$$

where the $\{c_j\}$ are dimensionless coefficients that may be $\mathcal{O}(1)$ that can have either sign. The effective cutoff $\Lambda$ for the new physics scale is connected to $\Lambda_j$ via $\Lambda_j \equiv \Lambda/|c_j|^{1/4}$.

In the present analysis we consider the following set of CP-conserving dimension-8 nTGC operators $(\mathcal{O}_{G+},\, \mathcal{O}_{G-},\, \mathcal{O}_{\tilde{B}W},\, \mathcal{O}_{\widetilde{BW}})$ [22, 23, 24]:

$$g\mathcal{O}_{G+} = \tilde{B}_{\mu\nu}W^{a\mu\rho}(D_\rho D_\lambda W^{a\nu\lambda} + D^\nu D^\lambda W^a_{\lambda\rho})\,, \tag{2a}$$
$$g\mathcal{O}_{G-} = \widetilde{B}_{\mu\nu}W^{a\mu\rho}(D_\rho D_\lambda W^{a\nu\lambda} - D^\nu D^\lambda W^a_{\lambda\rho})\,, \tag{2b}$$
$$\mathcal{O}_{\tilde{B}W} = \mathrm{i}H^\dagger \widetilde{B}_{\mu\nu}W^{\mu\rho}\,\{D_\rho, D^\nu\}H + \text{h.c.}\,, \tag{2c}$$
$$\mathcal{O}_{\widetilde{BW}} = \mathrm{i}H^\dagger\big(D_\sigma \widetilde{W}^a_{\mu\nu}W^{a\mu\sigma} + D_\sigma \widetilde{B}_{\mu\nu}B^{\mu\sigma}\big)D^\nu H + \text{h.c.} \tag{2d}$$

The nTGC vertex $Z\gamma V^*$ $(V=Z,\gamma)$ can be expressed in terms of nTGC form factors $(h_3^V,\, h_4^V)$ as follows [23, 24]:

$$\Gamma^{\alpha\beta\mu(8)}_{Z\gamma V*}(q_1,q_2,q_3) = \frac{e(q_3^2 - M_v^2)}{M_Z^2}\left[\left(h_3^V + \frac{h_4^V}{2M_Z^2}q_3^2\right)q_{2\nu}\epsilon^{\alpha\beta\mu\nu} + \frac{h_4^V}{M_Z^2}q_2^\alpha q_{3\nu}q_{2\sigma}\epsilon^{\beta\mu\nu\alpha}\right]. \tag{3}$$

By matching this nTGC form factor formulation with the corresponding gauge-invariant dimension-8 nTGC operators, a nontrivial form factor relationship can be derived, $h_4^Z = \frac{c_W}{s_W}h_4^\gamma$ [23, 24], and henceforth we will denote $h_4^Z \equiv h_4$ for simplicity. Thus there are three independent form-factor parameters $(h_4, h_3^Z, h_3^\gamma)$ [23, 24], which can be determined by matching the gauge-invariant dimension-8 nTGC operators $(\mathcal{O}_{G+}, \mathcal{O}_{G-}, \mathcal{O}_{\tilde{B}W}, \mathcal{O}_{\widetilde{BW}})$ in the broken phase of the electroweak gauge group $\mathrm{SU}(2)_L\otimes\mathrm{U}(1)_Y$. The form factors $(h_4, h_3^Z, h_3^\gamma)$ are connected as follows to the cutoff scales $(\Lambda_{G+}, \Lambda_{G-}, \Lambda_{\tilde{B}W}, \Lambda_{\widetilde{BW}})$ of the corresponding dimension-8 nTGC operators [23, 24]:

$$h_4 = -\frac{1}{[\Lambda^4_{G+}]}\frac{v^2M_Z^2}{s_Wc_W}\,, \tag{4a}$$
$$h_3^Z = \frac{1}{[\Lambda^4_{\tilde{B}W}]}\frac{v^2M_Z^2}{2s_Wc_W}\,, \tag{4b}$$
$$h_3^\gamma = -\frac{1}{[\Lambda^4_{G-}]}\frac{v^2M_Z^2}{2c_W^2} = -\frac{1}{[\Lambda^4_{\widetilde{BW}}]}\frac{v^2M_Z^2}{s_Wc_W}\,, \tag{4c}$$

where we denote $[\Lambda_j^4] = \text{sign}(c_j)\Lambda_j^4$ and $[\Lambda_j^{-4}] = \text{sign}(c_j)\Lambda_j^{-4}$.

In the following, we perform a systematic detector-level simulation and analysis of sensitivities to the nTGC dimension-8 effective operators via measurements of the nTGC form factors in the reaction $e^+e^- \to Z\gamma$ at the CEPC.

### 2.2 CEPC Detector

The Circular Electron Positron Collider (CEPC) [25] is an international research facility proposed in China that is designed to meet the requirements of various physics studies, especially precision measurements. CEPC has well-defined momentum and energy, as well as a clean experimental environment in comparison with hadron colliders. Thus it is possible to reconstruct angular variables in a more accurate way. Hence, CEPC is an ideal facility for probing new physics beyond the SM.

### 2.3 Simulation

For the purpose of this analysis, signal events are generated using MadGraph5_aMc@NLO [26] and Pythia8 [27], using the nTGC formulation described in Section 1. This nTGC formulation is implemented and imported to MadGraph5_aMc@NLO using FeynRules for nTGC event production at the matrix element level at leading order. Pythia8 is used for parton showering, fragmentation and describing the underlying events.

We analyze the contributions of three nTGC form factors $(h_4\, h_3^Z, h_3^\gamma)$ with benchmark choices shown in the second row of Table 1 and the corresponding cross sections shown in its third row. The dependence of the $Z\gamma$ cross section on the nTGC form factors $h_j$ (and the corresponding cutoff scale $\Lambda_j$) can be expressed as follows:

$$\sigma_{Z\gamma} = \sigma_0 + \bar{\sigma}_1 h_j + \bar{\sigma}_2 h_j^2 = \sigma_0 + \tilde{\sigma}_1[\Lambda_j^{-4}] + \tilde{\sigma}_2\Lambda_j^{-8}\,, \tag{5}$$

where $\sigma_0$ is the SM contribution, $\bar{\sigma}_1$ or $\tilde{\sigma}_1$ arises from the interference term between the nTGC and SM contributions, and $\bar{\sigma}_2$ or $\tilde{\sigma}_2$ corresponds to the squared nTGC contributions. In the above we use the notation $[\Lambda_j^{-4}] = \text{sign}(c_j)\Lambda_j^{-4}$ as defined below Eq.(4).

| Form Factors | $h_4$ | $h_3^\gamma$ | $h_3^Z$ | $(h_4,\, h_3^\gamma)$ | $(h_4,\, h_3^\gamma)$ | $(h_3^\gamma,\, h_3^Z)$ |
|---|---|---|---|---|---|---|
| $h_i^V$ | 0.28 | 0.16 | 0.36 | (0.83, 0.49) | (0.83, 1.07) | (0.49, 1.07) |
| $\sigma_{Z\gamma}$ (fb) | 2616 | 2752 | 2712 | 3732 | 3613 | 5120 |

Table 1: Benchmark values for the form factors $(h_4\, h_3^Z, h_3^\gamma)$ (second row) and the corresponding cross sections for $Z\gamma$ production (third row).

In Table 1, each nTGC benchmark consists of three contributions: the SM term, the interference term between the SM and nTGC, and the squared nTGC term. We achieve accurate sample production by decomposing the $Z\gamma$ cross section into these three terms and generating each term independently. We have checked our procedure by comparing distributions obtained using this decomposed mode with a direct simulation of their combination. We show good agreement between these two approaches in Fig. 3, and more cross-check plots can be found in Figs. 10 - 11 in the Appendix.

The package `WHIZARD` [28] is used to simulate background events. All background samples considered in this analysis can be divided into three categories: the 2-fermion background

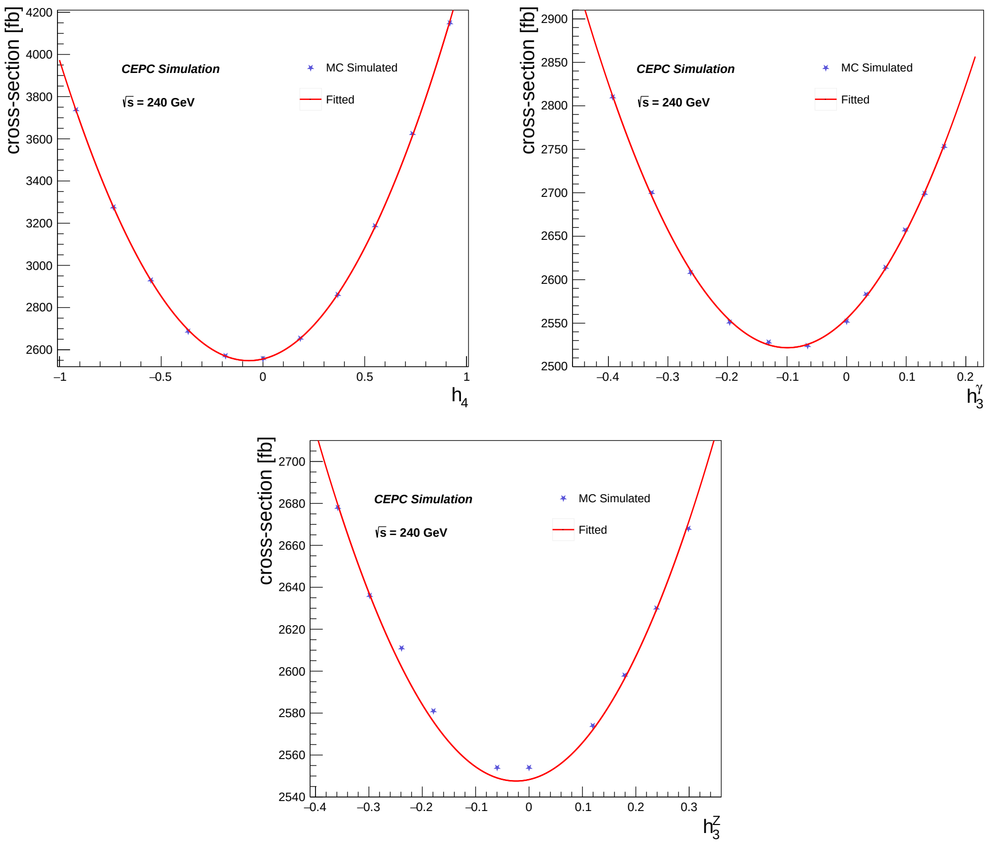


Figure 2: Cross sections as functions of the form factors $h_4, h_3^{\gamma}$, and $h_3^{Z}$. The interrelation between cross-sections and form factors is evaluated by varying the parameter values, which align closely with the polynomial equation (5). The solid blue stars represent the outputs from MadGraph_aMc@NLO simulations, while the red solid lines indicates the curve fits extracted through parametrisations corresponding to equation (5).

(which is dominant), the 4-fermion backgrounds, and the resonant Higgs backgrounds. Detailed information on the background processes is given in Table 9 of the Appendix.

The simulation of the detector response is handled by MokkaPlus [29], a GEANT4 [30]-based framework. We perform the full detector simulation for the signal process, whereas the background processes are simulated using Delphes [31].

### 2.4 Analysis Strategy

The CEPC detector adopts the Particle Flow Algorithm (PFA) [32] for event reconstruction, using the dedicated toolkit Arbor [33], which collects tracks and hits from the calorimeter and composes the Particle Flow Objects (PFOs) with its clustering and matching modules. The CEPC detector acts like a "camera" that tracks every particle collision. It is not possible to observe all the particles directly in the collisions because some of them decay promptly or do not interact with the detector. However, if they decay to stable particles or interact with the apparatus, they leave signals in the subdetectors. These signals are used to reconstruct the decay products or to infer their presence as physics objects. These objects can be photons, electrons, muons, jets, missing energy, etc.

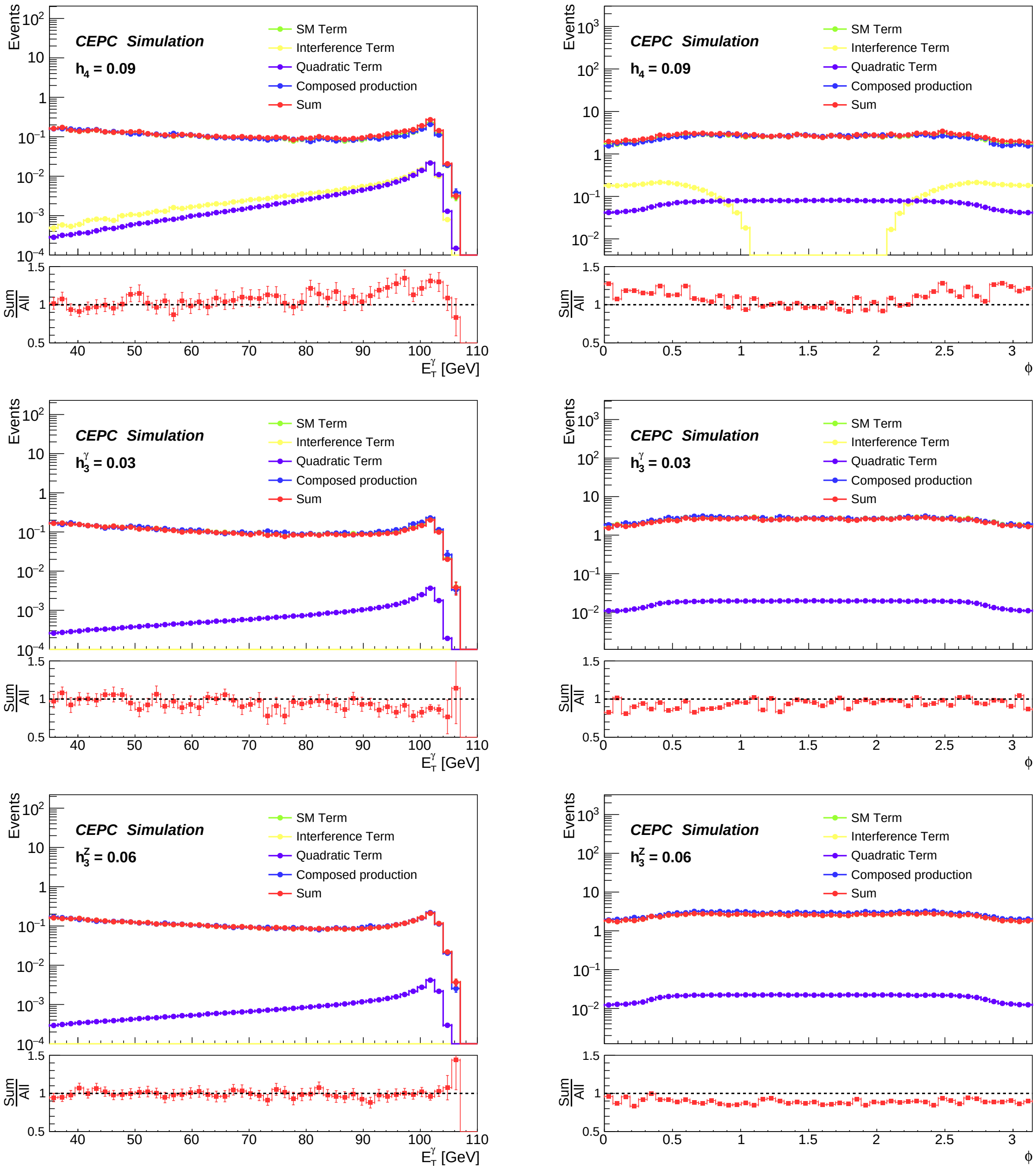


Figure 3: Consistency test for the evaluation of the effects of the dimension-8 operators $\mathcal{O}_{G+}, \mathcal{O}_{G-}$ and $\mathcal{O}_{\tilde{B}W}$. In order to reach higher statistics and accuracy we decomposes the cross-sections by generating the SM, interference and quadratic terms separately. The three terms generated in this decomposed mode are summed up and compared with independent calculations of the total cross-sections, and good consistency is observed.

In this analysis, photons are identified in Arbor using shower shape variables obtained from the high granularity calorimeter without any matched tracks. Leptons ($e^{\pm}, \mu^{\pm}$) are identified by a track-matched particle. A likelihood-based algorithm, LICH [34], is implemented in Arbor to separate electrons, muons, and hadrons. The overall lepton identification efficiencies [34] for electrons and muons are 99.7% and 99.9% respectively, where mis-identification rates are lower than 0.07%. To reconstruct fully electrons and muons, and to make sure no ambiguity exists, a lepton isolation criterion [35] is also applied by requiring $E_{\rm cone}^2 < 4E_\ell + 12.2$, where $E_{\rm cone}$ is the energy within a cone with $\cos\theta_{\rm cone} < 0.98$ around the lepton and $E_\ell$ is the energy of the lepton. Here $E_\ell$ and $E_{\rm cone}$ are measured in GeV. The polar angle between two selected leptons systems is required to be within the range $|\cos\theta_{\mu^+\mu^-}| < 0.81$ and $|\cos\theta_{e^+e^-}| < 0.71$ so as to ensure that the selected leptons are isolated. Jets are also reconstructed by Arbor, after removing isolated leptons and photons so as to avoid mis-reconstruction due to lepton or photon constituents. A list of object definitions is shown in Table 2.

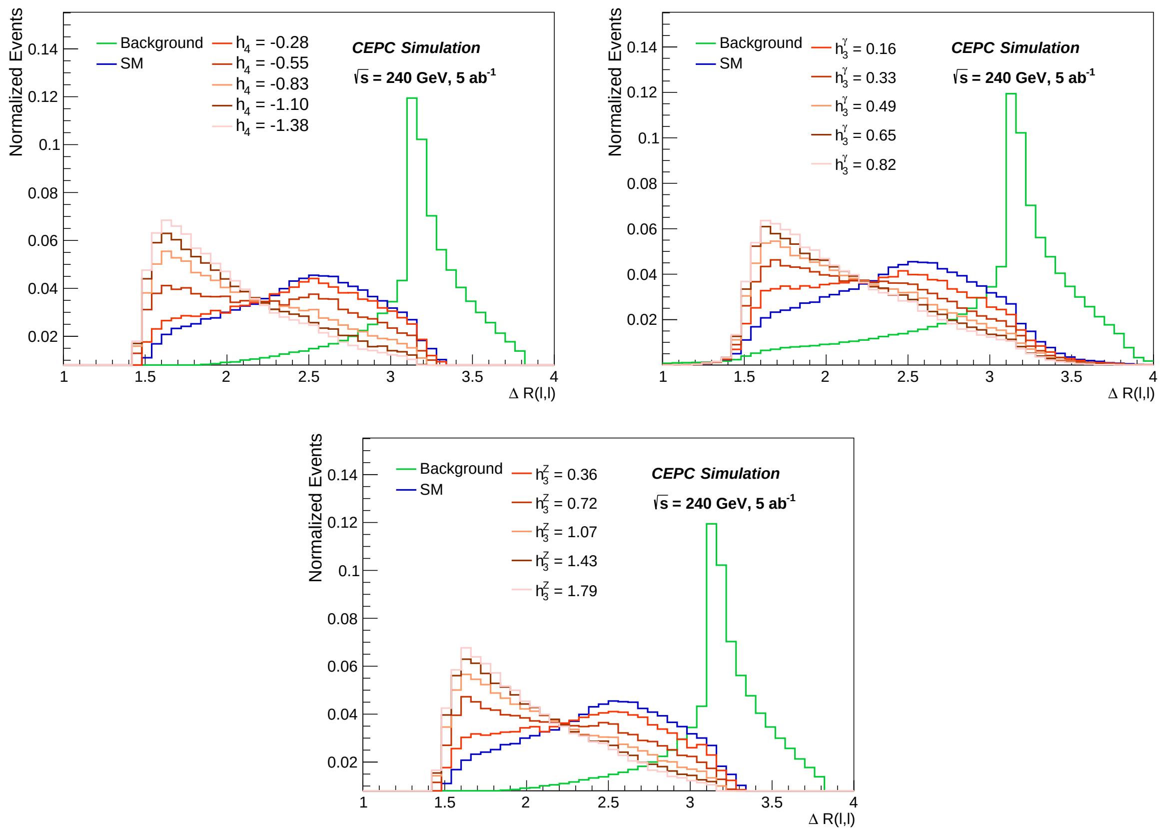


Figure 4: Normalized distributions of the separation $\Delta R(\ell,\ell)$, including the effects of different dimension-8 operators. The performance of $\Delta R(\ell,\ell)$ for leptons originating from different sources exhibits significant variations. The distinctions in $\Delta R(\ell,\ell)$ between different processes play pivotal roles in enhancing signal detection and minimizing background contributions.

This analysis is based on events with at least one photon and a pair of leptons with the same flavor and opposite signs (electron and muon). The event selections summarised in Table 3 are applied to improve the signal significance.

The event selections are optimised according to the requirements of the formulation in [21]. We first request that no selected jets be left in the signal events, so as to remove higher-order corrections appearing at Next-to-Leading Order (NLO) and beyond as much as possible, and to ensure that cross-section enhancement comes from nTGC, not higher-order SM corrections or other SM jet backgrounds. This is an effective cut to remove other SM backgrounds and to improve sensitivity. In this scenario, we also require that two leptons must come from the same Z boson by requiring the invariant mass difference between the di-lepton system and the on-shell Z boson mass be smaller than 10 GeV. Events with final-state radiation photons (FSR)

| Objects | Requirements |
|---|---|
| Electrons | $p_T > 15$ GeV, $\lvert\cos\theta\rvert$ <0.969<br>$E^2_{\text{cone}} < 4E_\ell + 12.2$<br>$\lvert\cos\theta_{e^+e^-}\rvert < 0.71$<br>(Overlap removal) $\Delta R(e,j) > 0.4$, $\Delta R(e,\mu) > 0.4$ |
| Muons | $p_T > 15$ GeV, $\lvert\cos\theta\rvert$ <0.969<br>$E^2_{\text{cone}} < 4E_\ell + 12.2$<br>$\lvert\cos\theta_{\mu^+\mu^-}\rvert < 0.81$ |
| Photons | $p_T > 30$ GeV, $\lvert\cos\theta\rvert$ <0.969<br>(Overlap removal) $\Delta R(\gamma,e) > 0.4$, $\Delta R(\gamma,\mu) > 0.4$ |
| Jets | $p_T > 25$ GeV, $\lvert\cos\theta\rvert$ <0.969<br>(Overlap removal) $\Delta R(j,\gamma) > 0.4$, $\Delta R(j,e) > 0.4$ |

Table 2: Summary of selection cuts on leptons, photons, and jets. These basic cuts [35] are independent of generator implementation and are needed for selecting stable particles as well as the analysis of complex event topologies.

are suppressed by requiring that the sum of the invariant mass of the leptons and the invariant mass of leptons and photon is greater than twice the Z mass ($|m_{\ell\ell} + m_{ll\gamma}|$ >182 GeV). We also apply the cut $\Delta R(\ell,\ell) < 3$ to suppress background contributions as shown in Fig. 4. All the selections listed in Table 3 are required so as to make the correct transformation between the SMEFT and the Effective Vertex Theory formulated in [21].

| Variables | Cut |
|---|---|
| $N_{\text{lep}}$ | 2 signal OSSF leptons with leading lepton $p_T^{\text{lep}} > 30$ GeV |
| $N_{\text{pho}}$ | $\geq 1$ signal photon with $p_T^{\gamma} > 35$ GeV |
| $N_{\text{jet}}$ | 0 |
| $\Delta R(\ell,\ell)$ | $< 3$ |
| $m_{\ell\ell}$ | $\lvert m_{\ell\ell} - m_Z\rvert < 10$ GeV |
| $m_{\ell\ell} + m_{\ell\ell\gamma}$ | $> 182$ GeV |

Table 3: Summary of event selection cuts used in this analysis.

In this measurement the nTGC form factors are constrained by measurements of $e^+e^- \to Z(\to \ell^+\ell^-)\gamma$ where $\ell = e, \mu$. An event selection strategy is proposed based on the new form factor formulation and summarised in Tables 4 and 5, which display the signal cut-flow results including contributions of the SM, the interference term, and the quadratic term.

## 3 Systematics

We have considered several sources of systematic uncertainties, which can be grouped into two types: theoretical and experimental uncertainties. Both systematic uncertainties have been assigned to the expected signal yields and then propagated to the SMEFT fits.

| Variables | SM Backgrounds | SM $Z\gamma$ | $h_4$ | $h_3^\gamma$ | $h_3^Z$ |
|---|---|---|---|---|---|
| $N_{\text{pho}} \geqslant 1$ | 11712 | 1572 | 1629 | 1747 | 1710 |
| $N_{\text{lep}} = 2$ | 1152 | 587 | 624 | 696 | 675 |
| $N_{\text{jet}} = 0$ | 811 | 587 | 624 | 696 | 675 |
| $\Delta R(\ell,\ell) < 3$ | 698 | 548 | 585 | 656 | 634 |
| $\lvert m_{\ell\ell} - m_Z \rvert < 10\,\text{GeV}$ | 303 | 192 | 226 | 288 | 271 |
| $(m_{\ell\ell} + m_{\ell\ell\gamma}) > 182\,\text{GeV}$ | 300 | 192 | 226 | 288 | 271 |

Table 4: Cut-flow table for the nTGC form factors, enumerating the cross sections (in fb) after applying sequential selections and using the indicated event-topology requirements. The initial cross sections for each nTGC form factor are shown in Table 1. The implementation of these selections mitigates SM background contributions efficiently, whereas it preserves signal events.

| Variables | SM Backgrounds | SM $Z\gamma$ | $(h_4, h_3^\gamma)$ | $(h_4, h_3^Z)$ | $(h_3^\gamma, h_3^Z)$ |
|---|---|---|---|---|---|
| $N_{\text{pho}} \geqslant 1$ | 11712 | 1572 | 2614 | 2506 | 3811 |
| $N_{\text{lep}} = 2$ | 1152 | 587 | 1225 | 1178 | 1999 |
| $N_{\text{jet}} = 0$ | 811 | 587 | 1224 | 1176 | 1996 |
| $\Delta R(\ell,\ell) < 3$ | 698 | 548 | 1179 | 1126 | 1929 |
| $\lvert m_{\ell\ell} - m_Z \rvert < 10\,\text{GeV}$ | 303 | 192 | 751 | 717 | 1441 |
| $(m_{\ell\ell} + m_{\ell\ell\gamma}) > 182\,\text{GeV}$ | 300 | 192 | 751 | 717 | 1441 |

Table 5: Cut-flow table for pairs of nTGC form factors, enumerating the cross sections (in fb) after applying sequential selections and using the indicated event-topology requirements. The initial cross sections for the pairs of nTGC form factors are shown in Table 1. The implementation of these selections efficiently mitigates SM background contributions, whereas preserving signal events.

### 3.1 Signal Uncertainties

Unlike hadron colliders, only a few theoretical uncertainties influence the final measurement in lepton colliders such as CEPC. There is no impact from Parton Distribution Functions or $\alpha_s$, and little dependence on higher-order QCD corrections. For completeness, a 0.5% theoretical uncertainty [36] is assumed for the signal yields.

The experimental systematic uncertainties include those in the integrated luminosity, detector acceptance, trigger efficiency, object reconstruction and identification efficiency, object energy scale, and resolution. Luminosity in the CEPC detector is monitored by the LumiCal using the high-statistics BhaBha process, and a relative accuracy of 0.1% is expected to be achieved [36]. A well-described detector geometry is used in the simulation to provide a precise model of the detector acceptance and response. These uncertainties should be negligible in our analysis. The photon identification, reconstruction, and energy calibration rely on dedicated algorithms and real data. All these photon-related uncertainties are detailed and studied in the CEPC CDR [25] and controlled at the sub-percent level. We assume conservatively a 1% uncertainty in the the photon efficiency and 0.05% uncertainties [36] in the photon energy scale (PES) and resolution (PER). The lepton uncertainties are estimated by varying the Z boson mass selection by $\pm 1$ GeV. The differences between the varied and nominal signal yields will be considered lepton uncertainties, which are strongly related to the lepton selection criteria.

### 3.2 Background Uncertainties

The background yields are floated to consider background mis-modelling effects and uncertainties in cross section calculations. Fixed parameters are used to estimate uncertainties from different background processes. The event yields of the dominant 2-fermion background process are varied by ±5%, and the yields from other background processes (4 fermions and Higgs production) are varied by ±50%. These estimates are based on the recipe described in [35].

| Processes | Statistical | Theoretical | Experimental |
|---|---|---|---|
| $Z\gamma$ production ( $e^+e^- \to \ell^+\ell^-\gamma$ ) | 0.52% | 0.5% | (+2.96, -3.15)% |
| Fixed background | Dominant background: 5%<br>Other backgrounds: 50% | | |

Table 6: Overview of systematic uncertainties, estimated for $\sqrt{s} = 240\,\text{GeV}$ with integrated luminosity of $5\,\text{ab}^{-1}$. Those in the signal process are separated into statistical, theoretical, and experimental categories. The signal uncertainty is attributed predominantly to experimental factors, including resolution, identification efficiencies, and detector acceptance, collectively termed as “Experimental”. Background events are floated manually to account for potential uncertainties, according to the prescription in [35].

# 4 Results

The expected event yields for the SM $Z\gamma$ process and backgrounds are summarized in Table 7. The expected yields of SMEFT samples are propagated to the SMEFT fitting framework including all systematic uncertainties, and used to obtain sensitivities for the nTGCs.

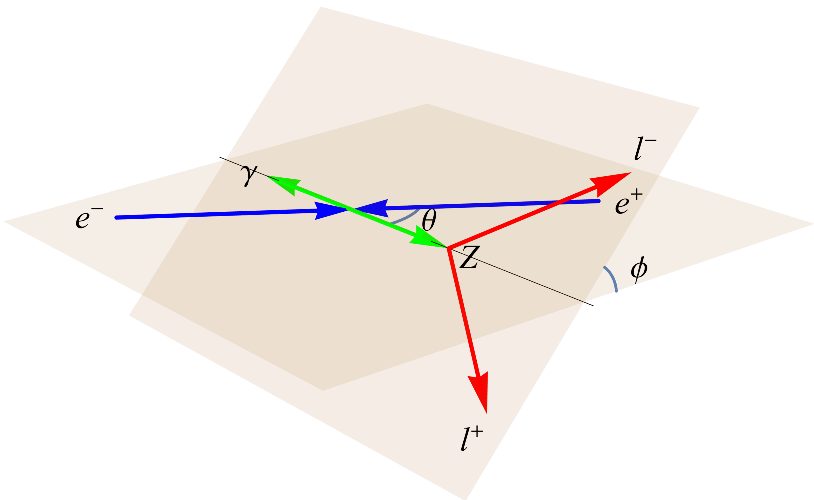


Figure 5: Kinematics in the $e^+e^-$ collision frame of the reaction $e^+e^- \to Z\gamma$ followed by the leptonic decays $Z \to \ell^+\ell^-$ [22][23]. We define $\phi$ as the angle between the scattering plane and the decay plane of the $Z$ in the $\ell^+\ell^-$ center-of-mass frame, and $\theta$ is the polar scattering angle between the directions of the outgoing $Z$ and initial state $e^-$.

| Processes | Event Numbers ($\times 10^3$) |
|---|---|
| SM $Z\gamma$ production | $961.4^{+29.3}_{-31.1}$ |
| 2-fermion background | $1491.3 \pm 74.6$ |
| 4-fermion background | $2.0 \pm 1.0$ |
| Higgs background | $2.0 \pm 1.0$ |
| Total yield | $2456.7^{+80.1}_{-80.8}$ |

Table 7: SM event yields and uncertainties ($\times 10^3$), extracted under $\sqrt{s} = 240\,\text{GeV}$ with integrated luminosity of $5\,\text{ab}^{-1}$. The expected event yields, incorporating both electron and muon channels, are extracted from the event topology-based analysis described in the text. The estimates include both statistical and systematic uncertainties.

A binned profile-likelihood fit is performed to set upper limits on the Wilson coefficients for dimension-8 operators at the 95% Confidence Level (C.L.). For this purpose we use the EFT fitting framework EFT-fun [37] to set 1- and 2-dimensional limits on nTGC parameters, individually and in parameter planes to exhibit their correlations. All the statistical and systematic uncertainties introduced in Section 3 are propagated to the EFT-fun [37] framework. The kinematic variables $\phi$ and $\theta$ illustrated in Fig. 5 are used in this measurement. The interference between SM and pure BSM contributions can be inferred directly from measuring these two variables, which enables better sensitivities for the nTGC coefficients.

Table 8 summarises the sensitivity reaches at the 95% CL for the new physics scales $\Lambda_i$ as obtained from the expected constraints on the associated form factors derived from the SMEFT dimension-8 coefficients given in the Effective Vertex Approach in Eq. (4), with all the systematic uncertainties taken into account. The constraints on the form factors derived in the Effective Vertex Approach are shown in Fig. 6 and the corresponding constraints on the operator scales within the SMEFT framework are shown in Fig. 7. Both figures highlight the central 95 % C.L range of the integral over the likelihood distribution, while values outside this range are excluded at this level. These depictions of the expected constraints on both the form factors and corresponding dimension-8 operator coefficients within the SMEFT framework offer a comprehensive understanding of the sensitivities to individual higher-dimensional operators.

| Form Factors | Expected limits | New Physics Scales | Expected limits (TeV) |
|---|---|---|---|
| $h_4$ | $[-5.6,\, 5.5]\times 10^{-4}$ | $\Lambda_{G+}$ | 1.21 |
| $h_3^\gamma$ | $[-2.3,\, 2.1]\times 10^{-3}$ | $\Lambda_{G-}$ | 0.62 |
| $h_3^Z$ | $[-3.9,\, 3.9]\times 10^{-3}$ | $\Lambda_{\tilde{B}W}$ | 0.63 |
| | | $\Lambda_{\widetilde{BW}}$ | 0.85 |

Table 8: Sensitivity reaches for the new physics scales $\Lambda_i$ and the form factors $(h_4,\, h_3^\gamma,\, h_3^Z)$ at the 95% C.L., which are obtained by analyzing the $\ell^+\ell^-\gamma$ channels with a benchmark luminosity of $5\,\text{ab}^{-1}$ and collision energy $\sqrt{s} = 240\,\text{GeV}$.

In adition to these 1-dimensional limits, we have also studied the constraints on different pairs of form factors, so as to understand their allowed correlations. Constraints in 2-dimensional planes are displayed as contour plots in Fig. 9. The solid lines in these plots represent the

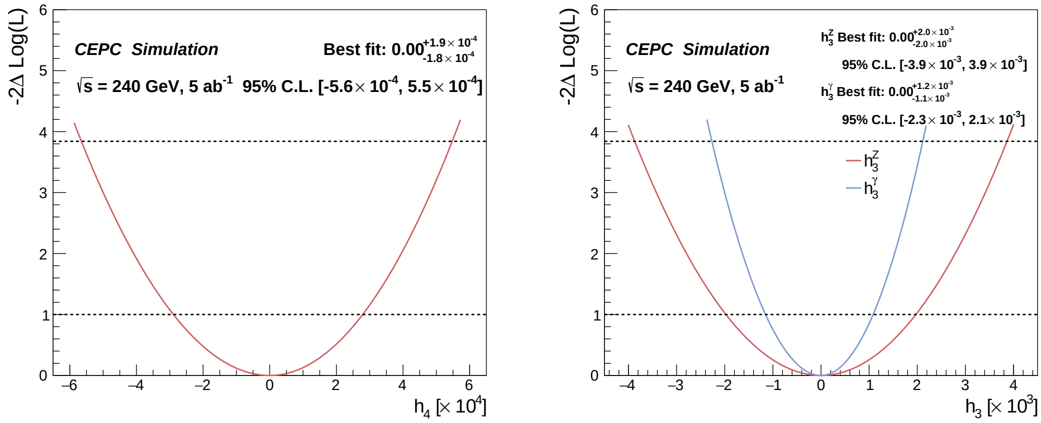


Figure 6: Expected limits (95% C.L.) on the nTGC form factors ($h_4$, $h_3^Z$, $h_3^\gamma$) and $1\sigma$ ranges (dotted lines). The best fit values shown in the plots correspond to the best agreements with the SM predictions.

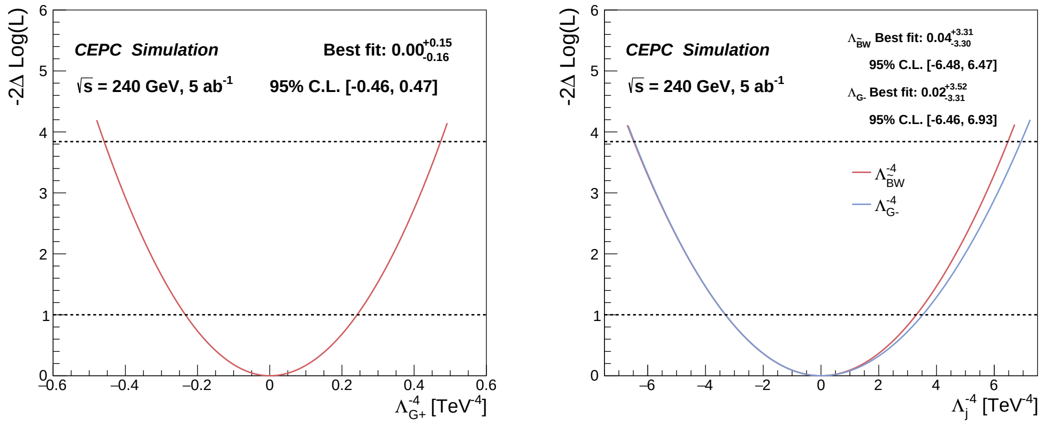


Figure 7: Expected limits (95% C.L.) on the coefficients $[\Lambda_j^{-4}]$ (in TeV$^{-4}$) of the dimension-8 nTGC operators ($\mathcal{O}_{G+}$, $\mathcal{O}_{G-}$, $\mathcal{O}_{\tilde{B}W}$) and $1\sigma$ ranges (dotted lines). The best fit values shown in the plots correspond to the best agreements with the SM predictions.

experimental constraints at 68% C.L., while the dashed lines indicate the 95% C.L. constraints, and areas outside the dashed (approximate) ellipses are excluded at the 95% C.L., taking into account all systematic uncertainties. We observe that the contour plots exhibit significant correlations between pairs of form factors.

As an alternative visualisation of our results, we have transformed the constraints from this form factor analysis to limits on the scales of the corresponding dimension-8 SMEFT operators in Fig. 8. The aspect ratios and orientations of the (approximately) elliptical contours indicate the degrees of correlation between pairs of operator coefficients.

The expected limits obtained in this paper are slightly better than the phenomenological results estimated theoretically in [21], despite the inclusion of all sources of systematic uncertainties, such as detector acceptance, object reconstruction, identification efficiencies and resolution. Our measurement is optimised using the BDTG method with multiple variables ($\phi*$, $\theta$ and $\theta*$ boosted into Z rest frame from the laboratory frame), which is an advance on the theoretical approach that used only a single variable ($\phi*$), it was to be expected that better sensitivities could be obtained. This method is documented in Appendix 5

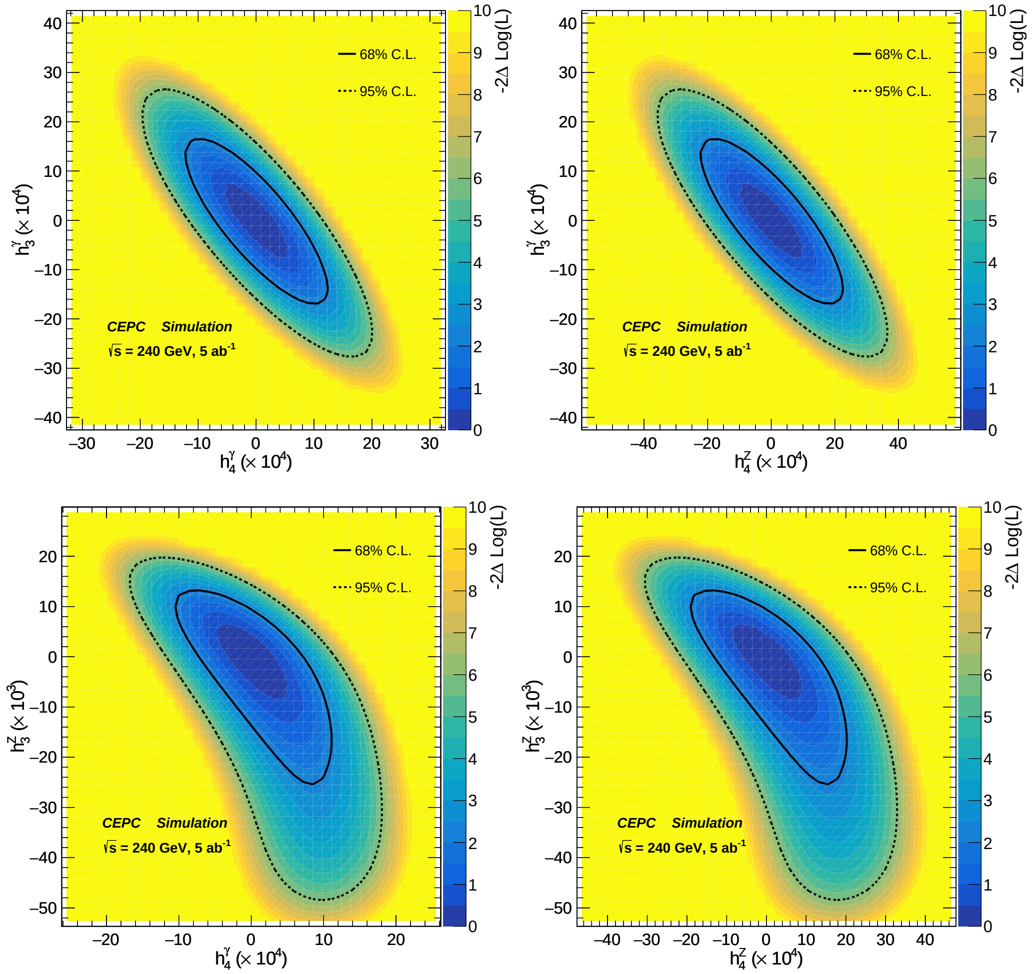


Figure 8: Correlation contours at the 68% and 95% C.L. for each pair of nTGC form factors.

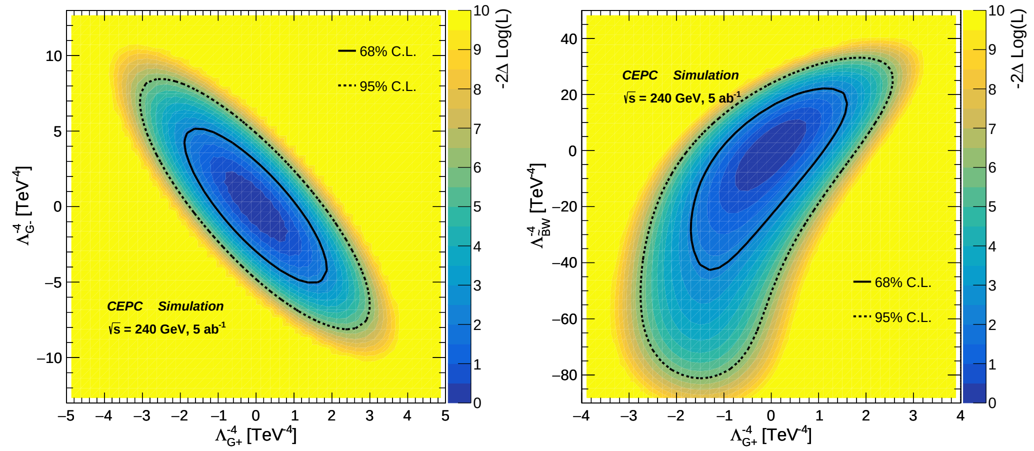


Figure 9: Correlation contours at the 68% and 95% C.L. for the cutoff scales $\Lambda_j$ of each pair of dimension-8 nTGC operators, where the axis labels are in units of $\text{TeV}^{-4}$.

## 5 Conclusions

Since nTGC vertices $Z\gamma V^*$ do not arise in the dimension-4 SM Lagrangian or in the SMEFT at the dimension-6 level, probing them from the contributions of dimension-8 operators provides a unique opportunity to explore new physics beyond the Standard Model (SM). We have investigated in this work the sensitivities to nTGCs through the reaction $e^+e^- \to \ell^+\ell^-\gamma$ (with $\ell = e, \mu$), performing a detector-level analysis and simulation for an experiment at the CEPC. Experiments at other $e^+e^-$ colliders with similar integrated luminosities and collision energies are expected to have similar sensitivities for probing the nTGCs.

Previous studies of the nTGC vertex $Z\gamma V^*$ via form factors are not consistent with spontaneously-broken electroweak gauge symmetry of the SM. Recently a new formulation of the nTGC form factor framework has been proposed [23, 24], which is consistently determined by mapping to the complete set of dimension-8 nTGC operators of the SMEFT and hence is compatible with the full electroweak gauge symmetry of the SM. It was found that extra dimension-8 nTGC operators are needed to establish the consistent mapping from the dimension-8 nTGC operators to the correct nTGC form factors [23, 24]. The consistent form factor expression for the CP-conserving nTGC vertex $Z\gamma V^*$ is shown in Eq.(3).

We have adopted the new nTGC form factor formula (3) to analyze the sensitivities to nTGCs in the $Z\gamma$ channel with $Z$ leptonic decays based on the benchmark luminosity $5\,\text{ab}^{-1}$ and $e^+e^-$ collision energy $\sqrt{s} = 240\,\text{GeV}$ at the CEPC. With these, we have obtained the nTGC sensitivity limits (95% C.L.) that take into account a single nonzero nTGC parameter at a time (as shown in Table 8), as well as the sensitivity contours (95% C.L.) for each pair of nTGC form factors or for each pair of cutoff scales of dimension-8 nTGC operators (as shown in Figs. 8 and 9).

Our results were obtained by a dedicated simulation with a realistic detector configuration and a full treatment of the systematic experimental uncertainties as well as statistical uncertainties. Our analysis employed a cut-based method using two experimental quantities, which provided sensitivities that are significantly stronger than the previous theoretical analyses that considered only single observables [21].

Table 8 shows that measurements of nTGCs at CEPC and other $e^+e^-$ Higgs factories have the potential to probe energy scales well beyond their center-of-mass energies, even exceeding a TeV in the most sensitive case of the nTGC operator $\mathcal{O}_{G+}$. These results are encouraging and confirm that nTGC measurements provide an interesting window to the dimension-8 new physics, extending the utility of the SMEFT beyond the dimension-6 level.

### Acknowledgments

The work of J.E. was supported in part by the United Kingdom STFC Grant ST/T000759/1. The work of HJH and RQX was supported in part by the NSFC Grants 12175136 and 11835005. RQX has also been supported by an International Postdoctoral Exchange Fellowship. We thank Gang Li, Yulei Zhang and Xuliang Zhu for discussions of the CEPC detector configuration.

# Appendix

### Background Samples

We summarize in Table 9 the cross sections of the background samples used in this analysis. We classify the background samples into 3 categories: 2 fermions, 4 fermions, and Higgs backgrounds. Each category contains multiple final states and the corresponding cross sections for the different channels as presented in this table.

| Processes | | Final States | $\sigma$ (fb) |
|---|---|---|---|
| 2 fermions | $\ell\ell$ | $e^+e^-/\mu^+\mu^-/\tau^+\tau^-$ | 34856.50 |
| | $\nu\nu$ | $\nu_e\bar{\nu}_e/\nu_\mu\bar{\nu}_\mu/\nu_\tau\bar{\nu}_\tau$ | 50499.51 |
| | $qq$ | $u\bar{u}/d\bar{d}/c\bar{c}/s\bar{s}/b\bar{b}$ | 54106.86 |
| 4 fermions | $WW$ (hadronic decay) | | 3825.46 |
| | $WW$ (leptonic decay) | | 403.66 |
| | $WW$ (semi-leptonic decay) | | 4846.99 |
| | $ZZ$ (hadronic decay) | | 516.67 |
| | $ZZ$ (leptonic decay) | | 67.81 |
| | $ZZ$ (semi-leptonic decay) | | 556.59 |
| Higgs | $e^+e^-H$ | $e^+e^-+H$ | 7.04 |
| | $\mu^+\mu^-H$ | $\mu^+\mu^-+H$ | 6.77 |
| | $\tau^+\tau^-H$ | $\tau^+\tau^-+H$ | 6.75 |
| | $\nu\nu H$ | $\nu_e\bar{\nu}_e/\nu_\mu\bar{\nu}_\mu/\nu_\tau\bar{\nu}_\tau+H$ | 46.29 |
| | $qqH$ | $u\bar{u}/d\bar{d}/c\bar{c}/s\bar{s}/b\bar{b}+H$ | 136.81 |

Table 9: Background samples used in the analysis of $e^+e^-\to Z\gamma$ with the collision energy $\sqrt{s}=240\,\text{GeV}$. The background samples are categorised into 3 groups: 2 fermions, 4 fermions, and Higgs backgrounds. Each group including multiple final states and the corresponding cross sections for the different channels are summarized in this table.

### Cross-Checks on the Decomposed Event Samples

In this part, we summarize cross-checks on the decomposed event samples.

We recall that 3 nTGC form factors ($h_4$, $h_3^Z$, $h_3^\gamma$) are studied in this work. In order to estimate the sensitivity to each form factor we allow just one form factor to be non-zero at each time, setting the others to zero, and in order to estimate the correlations between sensitivities to pairs of form factors we allow two form factors to be non-zero at each time, setting the third one to zero.

In general SMEFT analyses, there are two common methods for signal sample production, one is combined production (i.e., generating the SM and BSM terms together) and the other one is decomposed production (i.e., generating the SM and BSM terms separately). Since the extraction of the BSM process is limited by statistics, the decomposed production method is used in this analysis to generate the SM, interference and quadratic terms independently with higher accuracy. To check the reliability of the different production methods, cross-checks have been performed by comparing the distributions from different production modes, in which the sums of the decomposed samples are compared with the combined samples. We have verified good consistency for different kinematic variables between the two production modes. One-dimensional comparison plots for $\cos\phi$, $\phi$, $m_Z$, and $p_T^Z$ are shown in Fig. 10, and two-dimensional comparison plots for $\cos\phi, \phi, m_Z$ and $p_T^Z$ are shown in Fig. 11.

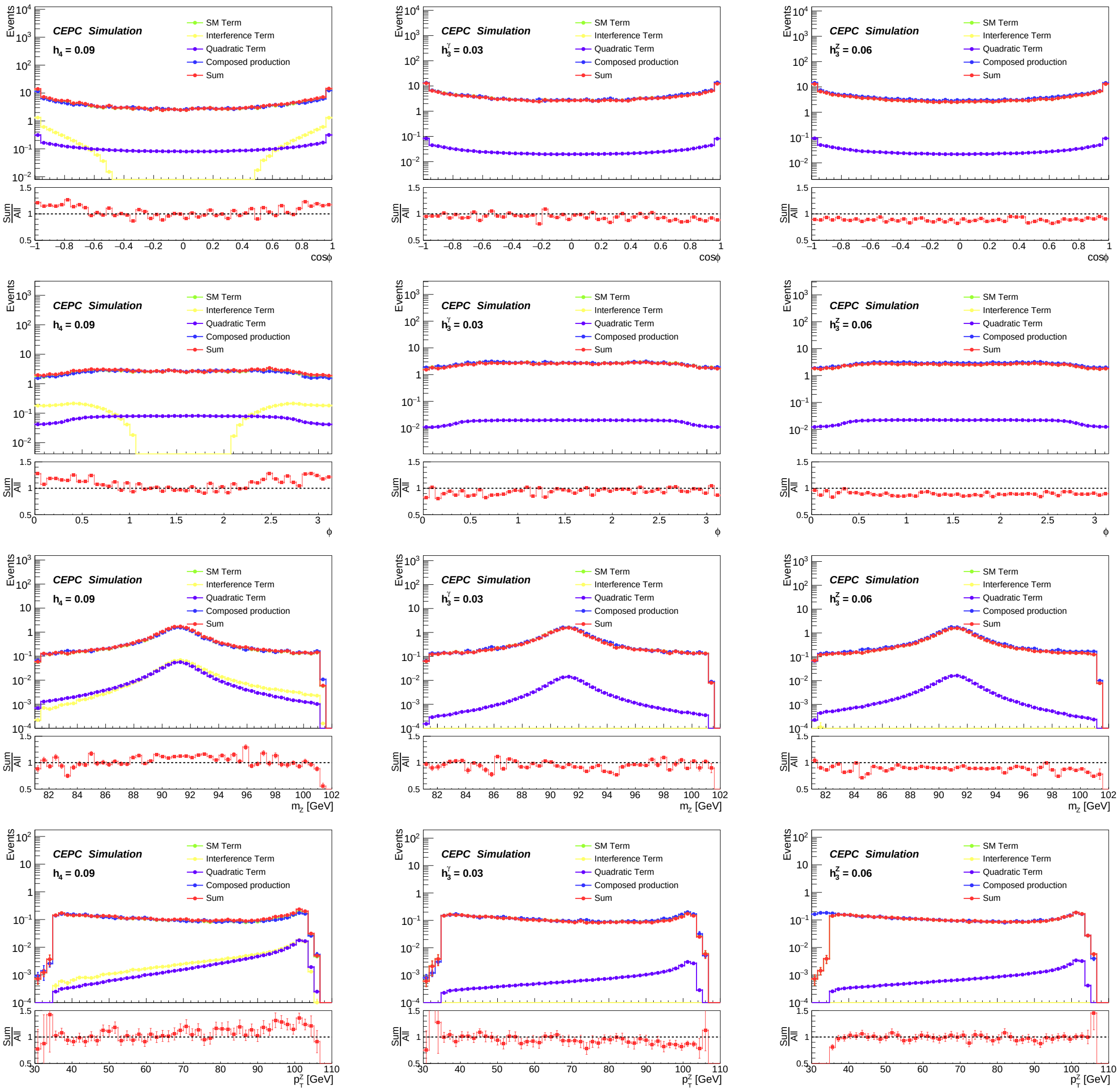


Figure 10: One-parameter comparisons and checks for the individual nTGC form factors ($h_4$, $h_3^Z$, $h_3^\gamma$) with different input values. A decomposed production mode is used in this analysis to generate the SM, interference and quadratic terms separately with high statistics and accuracy, and these three terms are summed up for comparison with the combined production mode. Good agreements are obtained for all the kinematic distributions.

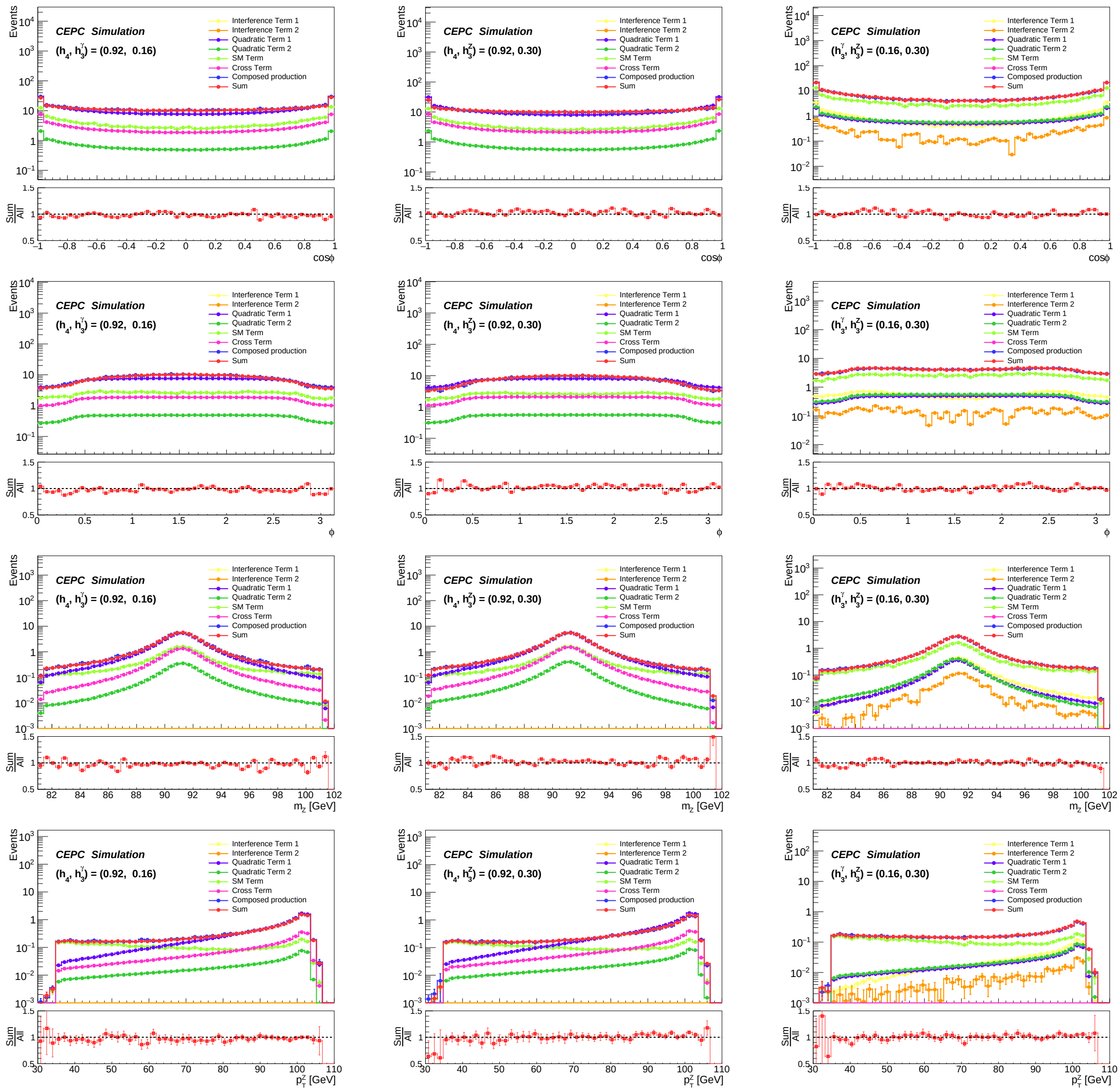

Figure 11: Two-parameter comparisons and checks for each pair of nTGC form factors $(h_i^V, h_j^V)$ with different input values. As in the one-parameter case, a decomposed production mode is used in this analysis to generate the SM, interference and quadratic terms separately with high statistics and accuracy, and these six terms are summed up for comparison with the combined production mode. Good agreement are obtained for all the kinematic distributions.

## Additional Kinematic Distributions

We compare the distributions of multiple kinematic variables from different processes and display them in the plots of Fig. 12. Differences between the SM $Z\gamma$ process, SM backgrounds and nTGC $Z\gamma$ processes (with various form factors) are shown clearly.

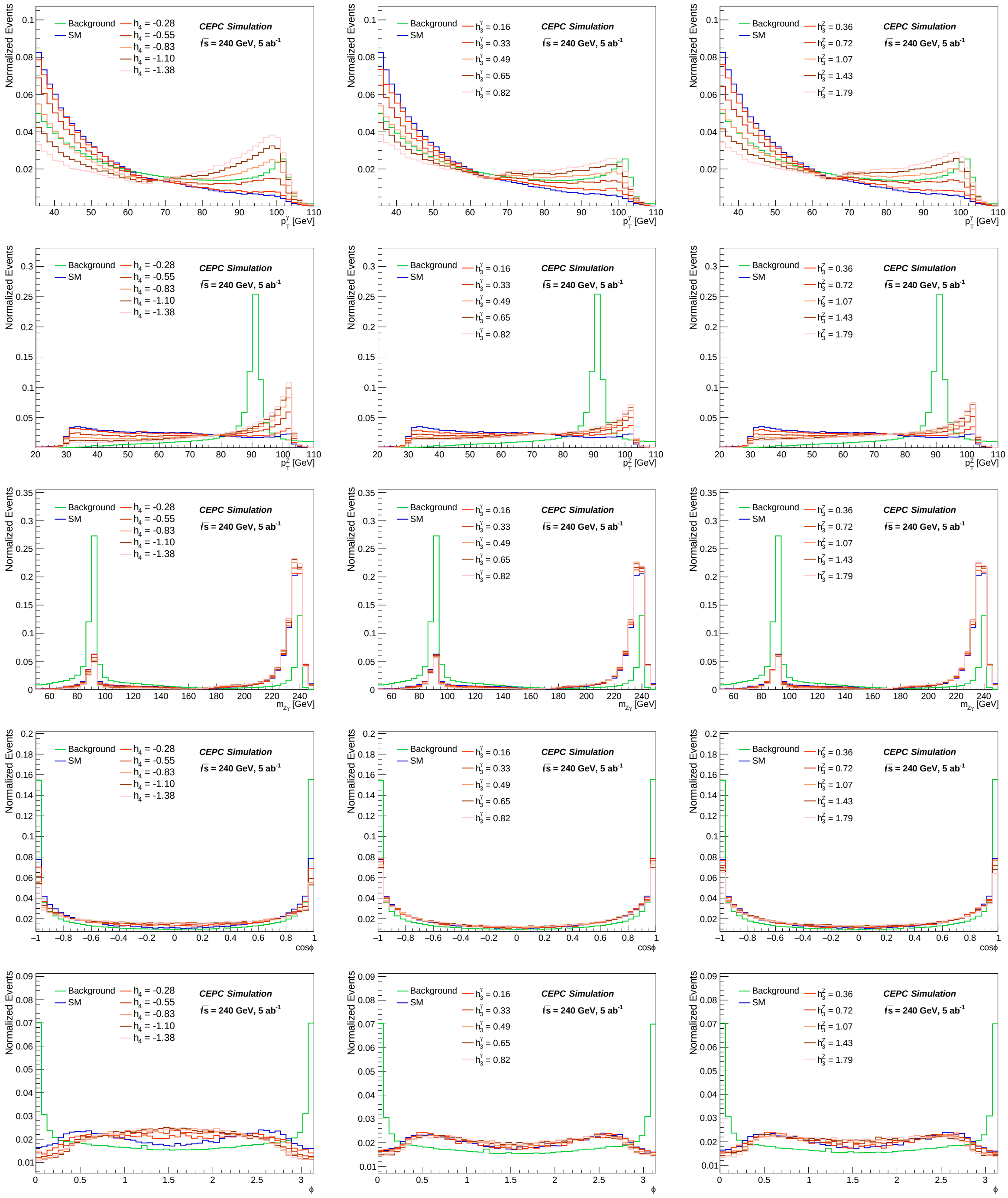

Figure 12: Distributions for kinematic variables and comparisons with the SM backgrounds for different signal processes. Samples including 2- and 4-fermion backgrounds and Higgs processes are compared with signal samples generated with varying values of the nTGC form factors. Clear differences between the SM $Z\gamma$, SM backgrounds and nTGC $Z\gamma$ processes are visible.

## BDT Optimisation

We use the Toolkit for Multivariate Data Analysis (TMVA) [38, 39], a component within the ROOT [40] framework for analyzing complex data sets, which provides a broad range of machine learning methods for classification and performance enhancement. Also, we employ the Boosted Decision Trees with Gradient boosting (BDTG) algorithm, which is a powerful tool for multivariate analysis with a broad range of classification algorithms. Its incorporation helps TMVA to process data more accurately and efficiently, making it a valuable asset for detailed data analysis.

The 2-dimensional distributions used in our multivariate study leverage measurements of three angles: $\phi$ denotes the angle between the scattering plane and the decay plane of $Z$ boson, $\theta$ is the polar angle of the outgoing $Z$ with respect to the initial electron as introduced in Fig. 5, and $\theta^*$ is the decay angle as measured in the $Z$ boson's rest frame. The distributions of these angles shown in Fig. 13-15 are key elements in this study.

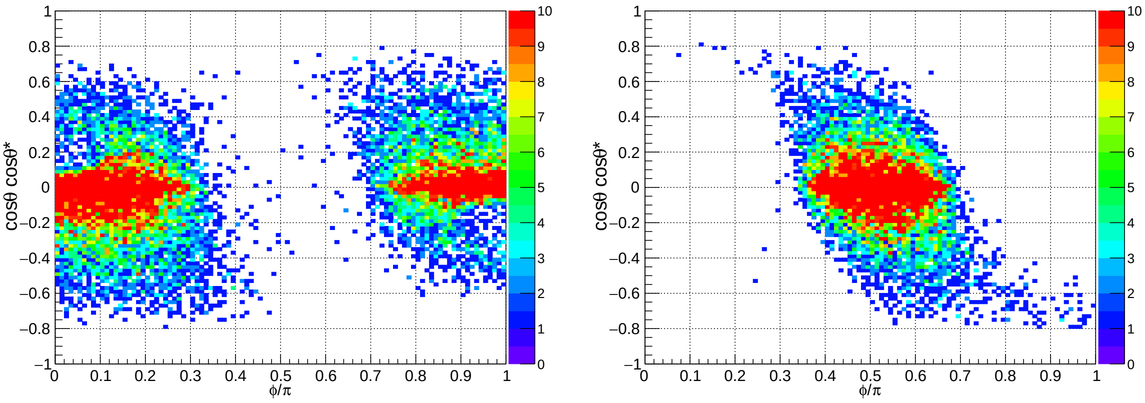


(a) $\bar{\sigma}_1(h_4) > 0$ (b) $\bar{\sigma}_1(h_4) < 0$

Figure 13: Normalized distributions of the angular variables employed to analyze the form factor $h_4$ by using simulated interference events. The left panel presents events with positive cross section in the interference term, whereas the right panel corresponds to events with negative cross section for the interference term.

The normalized 2-dimensional distributions of $\phi$ versus $\cos\theta\cos\theta^*$ demonstrate notable contrasts, indicative of the interference effects critical to constraining the nTGC form factors and the SMEFT parameters. The left panels of the Fig. 13-15 display events with positive interference cross-sections, whereas the right panels present those with negative values. These contrasts are instrumental in highlighting the influence of the interference terms and facilitating the extraction of the nTGC form factors.

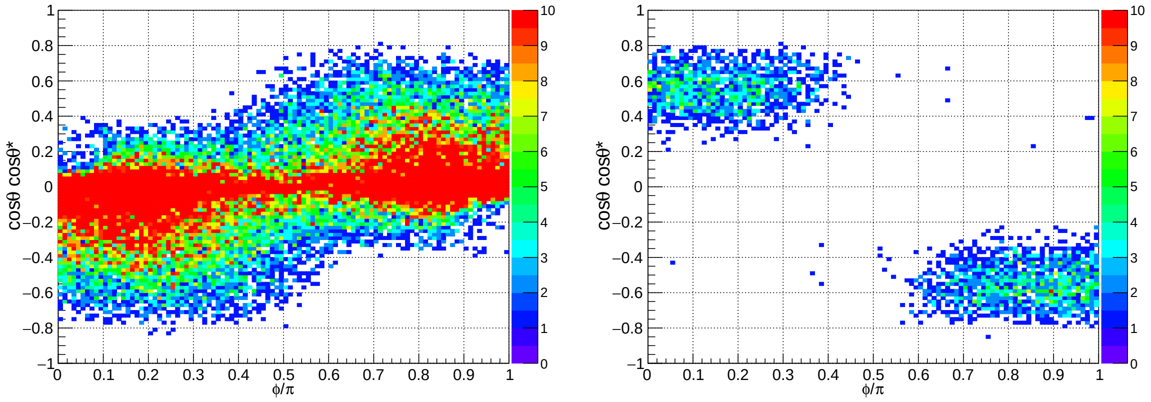


(a) $\bar{\sigma}_1(h_3^\gamma) > 0$ (b) $\bar{\sigma}_1(h_3^\gamma) < 0$

Figure 14: Normalized distributions of the angular variables employed to analyze the form factor $h_3^\gamma$ by using simulated interference events. The left panel presents events with a positive cross section for the interference term, whereas the right panel corresponds to events with a negative cross section for the interference term.

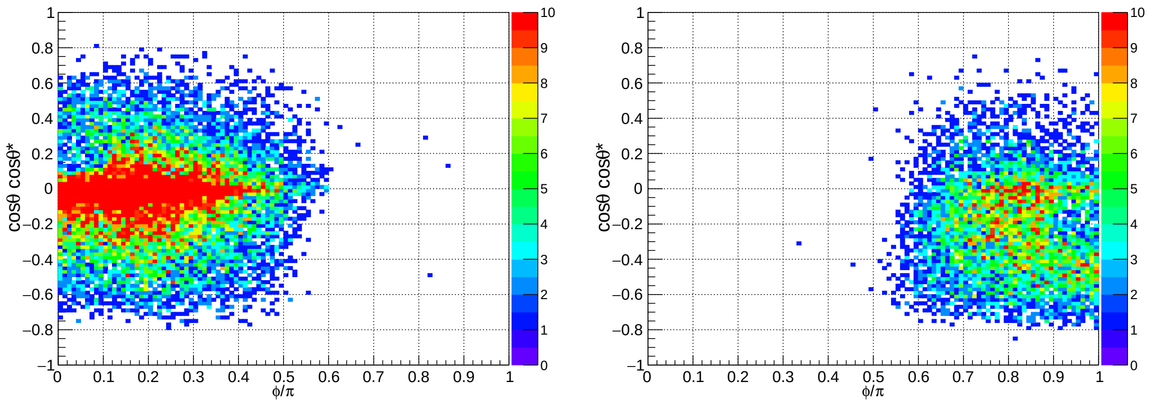


(a) $\bar{\sigma}_1(h_3^Z) > 0$ (b) $\bar{\sigma}_1(h_3^Z) < 0$

Figure 15: Normalized distributions of the angular variables employed to analyze the form factor $h_3^Z$ by using simulated interference events. The left panel presents events with a positive cross section for the interference term, whereas the right panel corresponds to events with a negative cross section for the interference term.

# References


[1] W. Buchmuller and D. Wyler. “Effective Lagrangian Analysis of New Interactions and Flavor Conservation”. Nucl. Phys. B 268 (1986), pp. 621–653.

[2] B. Grzadkowski et al. “Dimension-Six Terms in the Standard Model Lagrangian”. JHEP 10 (2010), p. 085. arXiv: 1008.4884 [hep-ph].

[3] G. F. Giudice et al. “The Strongly-Interacting Light Higgs”. JHEP 06 (2007), p. 045. arXiv: hep-ph/0703164.

[4] Christopher W. Murphy. “Dimension-8 operators in the Standard Model Eective Field Theory”. JHEP 10 (2020), p. 174. arXiv: 2005.00059 [hep-ph].

[5] Hao-Lin Li et al. “Complete set of dimension-eight operators in the standard model effective field theory”. Phys. Rev. D 104.1 (2021), p. 015026. arXiv: 2005.00008 [hep-ph].

[6] Alex Pomarol and Francesco Riva. “Towards the Ultimate SM Fit to Close in on Higgs Physics”. JHEP 01 (2014), p. 151. arXiv: 1308.2803 [hep-ph].

[7] Laure Berthier and Michael Trott. “Towards consistent Electroweak Precision Data constraints in the SMEFT”. JHEP 05 (2015), p. 024. arXiv: 1502.02570 [hep-ph].

[8] Laure Berthier and Michael Trott. “Consistent constraints on the Standard Model Effective Field Theory”. JHEP 02 (2016), p. 069. arXiv: 1508.05060 [hep-ph].

[9] Anke Biekötter, Tyler Corbett, and Tilman Plehn. “The Gauge-Higgs Legacy of the LHC Run II”. SciPost Phys. 6.6 (2019), p. 064. arXiv: 1812.07587 [hep-ph].

[10] John Ellis et al. “Top, Higgs, Diboson and Electroweak Fit to the Standard Model Effective Field Theory”. JHEP 04 (2021), p. 279. arXiv: 2012.02779 [hep-ph].

[11] Hong-Jian He, Jing Ren, and Weiming Yao. “Probing new physics of cubic Higgs boson interaction via Higgs pair production at hadron colliders”. Phys. Rev. D 93.1 (2016), p. 015003. arXiv: 1506.03302 [hep-ph].

[12] Shao-Feng Ge, Hong-Jian He, and Rui-Qing Xiao. “Probing new physics scales from Higgs and electroweak observables at $e^+e^-$ Higgs factory”. JHEP 10 (2016) 007 (). arXiv: 1603.03385 [hep-ph].

[13] Shao-Feng Ge, Hong-Jian He, and Rui-Qing Xiao. “Testing Higgs coupling precision and new physics scales at lepton colliders”. Int. J. Mod. Phys. A 31 (2016) 1644004, no.33 (). arXiv: 1612.02718 [hep-ph].

[14] J. de Blas et al. “Higgs Boson Studies at Future Particle Colliders”. JHEP 01 (2020), p. 139. arXiv: 1905.03764 [hep-ph].

[15] Tyler Corbett et al. “EWPD in the SMEFT to dimension eight”. JHEP 06 (2021), p. 076. arXiv: 2102.02819 [hep-ph].

[16] Tyler Corbett et al. “Impact of dimension-eight SMEFT operators in the electroweak precision observables and triple gauge couplings analysis in universal SMEFT”. Phys. Rev. D 107.11 (2023), p. 115013. arXiv: 2304.03305 [hep-ph].

[17] Ilaria Brivio et al. “O new physics, where art thou? A global search in the top sector”. JHEP 02 (2020), p. 131. arXiv: 1910.03606 [hep-ph].

[18] Gauthier Durieux et al. “The electro-weak couplings of the top and bottom quarks — Global fit and future prospects”. JHEP 12 (2019). [Erratum: JHEP 01, 195 (2021)], p. 98. arXiv: 1907.10619 [hep-ph].

[19] Jacob J. Ethier et al. “Combined SMEFT interpretation of Higgs, diboson, and top quark data from the LHC”. JHEP 11 (2021), p. 089. arXiv: 2105.00006 [hep-ph].

[20] Celine Degrande. “A basis of dimension-eight operators for anomalous neutral triple gauge boson interactions”. JHEP 2014.2 (2014). arXiv: 1308.6323 [hep-ph].

[21] John Ellis et al. “Probing the scale of new physics in the ZZ$\gamma$ coupling at e+e- colliders”. Chinese Physics C 44 (2020) 063106, no.6, (). arXiv: 1902.06631 [hep-ph].

[22] John Ellis, Hong-Jian He, and Rui-Qing Xiao. “Probing new physics in dimension-8 neutral gauge couplings at e+e- colliders”. Science China (Phys. Mech. & Astron.) 64 (2020) 221062, no.2, (). arXiv: 2008.04298 [hep-ph].

[23] John Ellis, Hong-Jian He, and Rui-Qing Xiao. “Probing neutral triple gauge couplings at the LHC and future hadron colliders”. Physical Review D 107 (2023) 035005, no.3, (). arXiv: 2206.11676 [hep-ph].

[24] Hong-Jian Ellis John He and Rui-Qing Xiao. “Probing neutral triple gauge couplings with $Z\gamma$ ($\nu\bar{\nu}\gamma$) production at hadron colliders”. Physical Review D 108 (2023) L111704, no.11, (). arXiv: 2308.16887 [hep-ph].

[25] The CEPC Study Group. *CEPC Conceptual Design Report: Volume 2 - Physics & Detector*. 2018. arXiv: 1811.10545 [hep-ex].

[26] Marco Zaro. “An introduction to MadGraph5_aMC@NLO”. (2022). URL: https://pcteserver.mi.infn.it/~mzaro/mg5amc-tif2-2022/tutorial-unimi-2022-tif.pdf.

[27] Torbjörn Sjöstrand, Stephen Mrenna, and Peter Skands. “A brief introduction to PYTHIA 8.1”. Computer Physics Communications 178.11 (2008). arXiv: 0710.3820 [hep-ph].

[28] Wolfgang Kilian, Thorsten Ohl, and Jürgen Reuter. “WHIZARD—simulating multi-particle processes at LHC and ILC”. The European Physical Journal C 71.9 (2011). arXiv: 0708.4233 [hep-ph].

[29] P. Mora de Freitas and H. Videau. “Detector simulation with MOKKA / GEANT4: Present and future”. *International Workshop on Linear Colliders (LCWS 2002)*. Aug. 2002, pp. 623–627. arXiv: 1902.06161v2 [physics.ins-det].

[30] S. Agostinelli et al. “GEANT4–a simulation toolkit”. Nucl. Instrum. Meth. A 506 (2003), pp. 250–303.

[31] Cheng Chen et al. “Fast simulation of the CEPC detector with Delphes”. (Dec. 2017). arXiv: 1712.09517 [hep-ex].

[32] Manqi Ruan et al. “Reconstruction of physics objects at the Circular Electron Positron Collider with Arbor”. The European Physical Journal C 78.5 (2018). arXiv: 1806.04879 [hep-ex].

[33] Manqi Ruan. “Arbor, a new approach of the Particle Flow Algorithm”. (2014). arXiv: 1403.4784 [physics.ins-det].

[34] Dan Yu et al. “Lepton identification at particle flow oriented detector for the future e+e- Higgs factories”. The European Physical Journal C 77.9 (2017). arXiv: 1701.07542 [physics.ins-det].

[35] Yu Bai et al. “Measurements of decay branching fractions of $H \to b\bar{b}/c\bar{c}/gg$ in associated ($e^+e^-/\mu^+\mu^-$)H production at the CEPC”. Chinese Physics C 44.1 (2020), p. 013001. arXiv: 1905.12903 [hep-ex].

[36] Fangyi Guo et al. "Expected measurement precision of the branching ratio of the Higgs boson decaying to the di-photon at the CEPC". Chin. Phys. C 47.4 (2023), p. 043002. arXiv: 2205.13269 [hep-ex].

[37] EFT-fun. URL: https://gitlab.cern.ch/eft-tools/eft-fun.

[38] *TMVA, Toolkit for Multivariate Data Analysis with ROOT*. URL: https://root.cern.ch/download/doc/tmva/TMVAUsersGuide.pdf.

[39] A. Hoecker et al. *TMVA - Toolkit for Multivariate Data Analysis*. 2009. arXiv: physics/0703039 [physics.data-an].

[40] *ROOT : analyzing petabytes of data, scientifically*. URL: https://root.cern/.